A particle simulation of current sheet instabilities under finite guide field

X. Y. Wang,[1] Y. Lin,[1] L. Chen,[2,3] and Z. Lin[2]
[1]*Department of Physics, Auburn University, Auburn, Alabama 36849, USA*
[2]*Department of Physics and Astronomy, University of California at Irvine, Irvine, California 92697, USA*
[3]*Institute for Fusion Theory and Simulation, ZheJiang University, Hang Zhou, ZheJiang 310058, China*

(Received 28 February 2008; accepted 13 May 2008; published online 3 July 2008)

The instability of a Harris current sheet under a broad range of finite guide field (B_G) is investigated using a linearized (δf) gyrokinetic electron and fully kinetic ion particle simulation code. The simulation is carried out in the two-dimensional plane containing the guide field along y and the current sheet normal along z. In this particle model, the rapid electron cyclotron motion is removed, while the realistic mass ratio m_i/m_e, finite electron Larmor radii, and wave-particle interactions are kept. It is found that for a finite $B_G/B_{x0} \leqslant 1$, where B_{x0} is the asymptotic antiparallel component of magnetic field, three unstable modes, i.e., modes A, B, and C, can be excited in the current sheet. Modes A and C, appearing to be quasielectrostatic modified two-stream instability/whistler mode, are located mainly on the edge of the current sheet. Mode B, on the other hand, is confined in the current sheet center and carries a compressional magnetic field (δB_y) perturbation along the direction of electron drift velocity. Our new finding suggests that mode B may contribute directly to the electron anomalous resistivity in magnetic reconnection. In the cases with extremely large $B_G/B_{x0} \gg 1$, the wave modes evolve to a globally propagating instability. The simulation shows that the presence of finite B_G modifies the physics of the current sheet significantly. © *2008 American Institute of Physics*. [DOI: 10.1063/1.2938732]

I. INTRODUCTION

Magnetic reconnection[1] is believed to be a fundamental physical process that plays an important role in both laboratory and natural plasmas. The reconnection process, which involves the connection of topologically different magnetic field lines, can take place at a current sheet that separates two different plasma regions with antiparallel magnetic field components. Anomalous resistivity in such a current sheet is thought to be crucial in achieving fast reconnection in collisionless plasmas. A number of microinstabilities, including Buneman, ion acoustic, electron cyclotron, lower-hybrid drift, drift kink, modified two-stream, whistler, and Weiber instabilities, have been proposed to produce such anomalous resistivity. However, in many applications of interest, the ratio of ion to electron temperatures $T_i/T_e > 1$, the ion drift speed $v_d \sim$ ion thermal speed v_{thi}, and the plasma β is finite, and thus some of these candidates for the source of resistivity are ineffective. The lower-hybrid drift instability (LHDI) and whistler modes are considered by some to be the most possible instabilities which provide the anomalous resistivity in a reconnection current sheet.

The low-hybrid drift, whistler, and modified two-stream instabilities (MTSI) have been studied for decades via theoretical analysis and numerical simulations. The electrostatic local theory by Krall and Rosenbluth[2] was the earliest linear theory that investigates the trapping instabilities in a small density gradient plasma. This theory was later extended to investigation of a Harris current sheet.[3] An electromagnetic local linear theory was derived by Davidson *et al.*[4] to study the LHDI. It was found that a high-beta plasma will stabilize the LHDI. Another candidate for the anomalous resistivity in current sheet is the modified two-stream instability,[5] which is driven in homogeneous plasmas by a large relative drift velocity between ions and electrons perpendicular to the magnetic field. While the maximum growth rate occurs at $k_\parallel = 0$ in the LHDI, the growth rate equals zero at $k_\parallel = 0$ and peaks at finite $k_\parallel/k$ in the MTSI. Local theory was also used to study the kinetic whistler mode driven by cross-field streaming.[6] It was argued that the whistler instability becomes the MTSI when $\beta \ll 1$ and $(k_\parallel/k)(m_i/m_e)^{1/2} \leqslant 1$.

Nonlocal electrostatic theory of inhomogeneous plasmas was developed and applied to analysis of the drift wave generated by a density gradient[7] and/or sheared magnetic field.[8] In the nonlocal kinetic theory derived by Huba *et al.*,[9] for a Harris current sheet without a guide magnetic field, it was found that the fastest growing LHDI is well localized at the edge of the current sheet. Meanwhile, Daughton[10,11] used a nonlocal electromagnetic theory to investigate the LHDI and drift kinetic instability (DKI) in a Harris current sheet with essentially a zero guide field. It was shown in their eigenfunctions that the long wavelength structure with $k_y\sqrt{\rho_i \rho_e} \sim 1$ has a significant electromagnetic component localized in the central region of the current sheet, while the fastest growing mode with $k_y \rho_e \sim 1$, mainly an electrostatic mode, is localized on the edge of the current sheet.

Nonlinear evolution of the LHDI and its role in anomalous resistivity were investigated by numerical simulations. The early full-particle simulation by Winske[12] described a long wavelength electromagnetic mode developed at the null point as a consequence of the nonlinear penetration of the LHDI, which is initially excited at the edge of the current sheet. In the simulation performed by Ozaki *et al.*[13] and Horiuchi and Sato,[14] LHDI generated away from the neutral

sheet in early period has sufficiently large growth rate and cannot penetrate into the current sheet center, implying that the LHDI cannot be directly responsible for anomalous resistivity in the neutral sheet. Instead, a drift kink instability, triggered in later period as a result of nonlinear deformation of the current sheet by LHDI, can create an anomalous resistivity.[15] Recent particle simulations by Daughton *et al.*[16] and Ricci *et al.*,[17] however, implied that LHDI generated in thin current sheet can penetrate into the central region and play an important role in the onset and nonlinear development of magnetic reconnection by heating electrons anisotropically and producing current bifurcation. In addition, the role of whistler mode instabilities in fast reconnection also attracted broad attention in recent simulations.[18–20] It was shown that in high-beta plasma, the whistler mode plays a key role in the physics of fast reconnection.[21]

Overall, previous theories and simulations on current sheet instabilities were focused mainly on the Harris current sheet without or with a very small guide field, which is certainly not the case in laboratory plasmas. Few investigated the instabilities at the current sheet center in the current sheet with a finite guide field. In the presence of a finite guide field B_G, the value of $k_\parallel/k$ in the instabilities may be nonzero, and the effects of finite $k_\parallel$ in anomalous resistivity may not be ignored. In addition, most of the fully kinetic particle simulations have adopted an artificial mass ratio m_i/m_e between ion and electron.

The roles of LHDI and whistler modes in a reconnection current sheet were also investigated in laboratory experiments and by satellite observations. Satellite observations indicated that LHDI is responsible for both large-amplitude electric field fluctuations[22,23] and the low-frequency electromagnetic turbulence[24] at a neutral sheet. The observation in MRX,[3,25] however, suggested that LHDI fluctuations are confined to the low-β edge of current sheet and do not play an essential role in determining the reconnection rate. Bale *et al.*[26] thought that the contribution of LHDI, observed in a reconnection current sheet at Earth's magnetopause, to plasma resistivity is negligible. On the other hand, many observations, both in laboratory and nature plasmas, found that whistler modes with frequency $\Omega_i < \omega < \Omega_e$ may play a significant role in fast reconnection. These whistler waves could be right-hand or linearly polarized,[27] propagating obliquely[28] or nearly perpendicular[29] to the reconnection field with phase speed around V_d, the relative drift speed between ions and electrons. Note that in laboratory experiments of MRX,[3,25,28] the guide field B_G is strong. As a whole, the roles of LHDI and other current sheet instabilities in reconnection are still controversial and under debate.

To overcome the numerical difficulty of the mass ratio (m_i/m_e) problem and address the physics of current sheet with a finite guide field, we have developed an innovative gyrokinetic electron and fully kinetic ion (GKe/FKi) particle simulation model.[30] In this paper, we use the newly developed GKe/FKi model to investigate instabilities in a two-dimensional (2D) Harris current sheet under a finite guide field B_G. In this model, the electron dynamics is determined by the gyrokinetic (GK) equations, in which fast electron gyromotion and Langmuir oscillations are removed from the dynamics, while ions obey the fully kinetic (FK) Vlasov equation. The microscopic physics and the global Alfvén scale dynamics in magnetic reconnection can be solved simultaneously with a realistic m_i/m_e ratio. Note that the relevant electromagnetic compressional waves are fully covered in our model. This model is particularly suitable for the dynamics with wave frequency $\omega < \Omega_e$ and wave number $k_\parallel < k_\perp$. Unlike the studies by Daughton,[11] our simulation plane contains the guide field and the current sheet normal, and thus instabilities with $k_\parallel \neq 0$ are expected to exist.

As a first step of our systematic study, in this paper, we linearize the GKe/FKi code using a δf method,[31] and present results of microinstabilities in the Harris current sheet based on the linearized GKe/FKi model. Note that a special case with a small guide field was studied using a purely electrostatic GKe/FKi δf simulation code, and the results were found to agree well with a linear local theory.[32] The fully electromagnetic δf scheme is utilized in this paper for general cases with a broad parameter range. The outline of the paper is given below. The GKe/FKi δf model is described in Sec. II. The simulation results for cases of a small to moderate guide field are presented in Sec. III. A case with extremely large guide field is also briefly discussed. A summary is given in Sec. IV.

II. LINEARIZED (δf) GKe/FKi SIMULATION MODEL

Physics of many interesting kinetic processes requires resolving both the ion and electron time scales in an integrated global-scale system. For example, to understand the physics of collisionless magnetic reconnection, one needs to resolve finite electron Larmor radius effects, consider electron wave-particle resonance (i.e., Landau damping), and include electron's off-diagonal pressure terms, whereas the spatial and temporal scales of the reconnection process range from the short electron scales to global Alfvén scales. It is, however, rather difficult to include all the disparate temporal and spatial scales due to the constraints of available computing power (e.g., particle-in-cell codes and hybrid codes).

In our new GKe/FKi kinetic simulation model,[30] the electrons are treated as gyrokinetic particles. The rapid electron cyclotron motion is averaged out and thus removed, but finite electron Larmor radius effects are retained. This allows for efficient simulation runs for realistic proton-to-electron mass ratio. The model is particularly suitable for the processes in which the wave modes ranging from low Alfvén wave frequency to intermediate lower-hybrid frequency need to be incorporated. Wave modes relevant to many applications, e.g., magnetohydrodynamic modes, the obliquely propagating whistler/lower-hybrid waves, modified two-stream instabilities, and kinetic Alfvén waves, fall inside this range of dynamic scales. The simulation model has been successfully benchmarked for linear waves in uniform plasmas against analytical dispersion relation.[30]

In the present discussion, we extend the analysis by Lin *et al.*[30] to the case of inhomogeneous current sheet with a finite guide field. The initial equilibrium current sheet is assumed to be a Harris sheet. For the purpose of studies on linear properties of waves, the GKe/FKi code is linearized,

and the linear simulation results are presented. In the following, we first describe the simulation scheme of the GKe/FKi model in the δf approximation. The initial and boundary conditions for the Harris current sheet in GKe/FKi plasma are then described.

A. GKe/FKi scheme in δf approximation

We apply a linearized δf scheme to the GKe/FKi model described by Lin *et al.*,[30] in which the ions are treated as fully kinetic particles and the electrons are treated with gyrokinetic approximations. In the δf scheme, the ion motion in unperturbed orbit under the zeroth-order magnetic field is governed by the particle equations of motion

$$\frac{d\mathbf{v}}{dt} = \frac{q_i}{m_i}\mathbf{v}\times\mathbf{B}_0, \qquad \frac{d\mathbf{x}}{dt} = \mathbf{v}, \tag{1}$$

where m_i is the ion mass and q_i is the ion charge.

In the electromagnetic GK approximation, the gyrocenter equation of motion for the parallel electron momentum, i.e., $p_\parallel = m_e v_{e\parallel} + q_e \delta A_\parallel / c$, and the electron gyrocenter position, i.e., $\mathbf{R} = \mathbf{x} - \boldsymbol{\rho}$, in zeroth-order fields, are given[30] by

$$\frac{dp_\parallel}{dt} = -\mathbf{b}^*\cdot\mu\nabla\bar{B}, \qquad \frac{d\mathbf{R}}{dt} = v_{e\parallel}\mathbf{b}^* + \frac{c}{q_e\bar{B}}\bar{\mathbf{b}}\times\mu\nabla\bar{B}, \tag{2}$$

where q_e is the electron charge, $v_{e\parallel}$ is the electron parallel velocity, μ is the magnetic moment, $\bar{\mathbf{b}} = \bar{\mathbf{B}}/B_0$, and $\mathbf{b}^* = \bar{\mathbf{b}} + (v_{e\parallel}/\Omega_e)\bar{\mathbf{b}}\times(\bar{\mathbf{b}}\cdot\nabla)\bar{\mathbf{b}}$.

In the δf scheme, the perturbed density weighting functions, $W_i = \delta f_i/\bar{f}_i$ for the ions and $W_e = \delta F_e/\bar{F}_e$ for the electrons, are advanced in time according to

$$\frac{dW_i}{dt} = -\frac{q_i}{m_i}\left(\delta\mathbf{E} + \frac{1}{c}\mathbf{v}\times\delta\mathbf{B}\right)\cdot\frac{\partial \ln \bar{f}_i}{\partial \mathbf{v}_i}, \tag{3}$$

$$\frac{dW_e}{dt} = -\left[\bar{v}_{e\parallel}\delta\mathbf{b}^* + \delta v_{e\parallel}\bar{\mathbf{b}}^* + \frac{c\bar{\mathbf{b}}}{q_e\bar{B}}\times(q_e\langle\nabla\delta\phi^*\rangle)\right]\cdot\frac{\partial \ln \bar{F}_e}{\partial\mathbf{R}} + [\delta\mathbf{b}^*\cdot(\mu\nabla\bar{B}) + \bar{\mathbf{b}}^*\cdot(q_e\langle\nabla\delta\phi^*\rangle)]\cdot\frac{\partial \ln \bar{F}_e}{\partial p_\parallel}, \tag{4}$$

where $\delta\mathbf{b}^* = (\delta v_{e\parallel}/\bar{\Omega}_e)\bar{\mathbf{b}}\times(\bar{\mathbf{b}}\cdot\nabla)\bar{\mathbf{b}} - (\bar{v}_{e\parallel}\delta\Omega_e/\bar{\Omega}_e^2)\bar{\mathbf{b}}\times(\bar{\mathbf{b}}\cdot\nabla)\bar{\mathbf{b}}$, $\delta v_{e\parallel} = -q_e\delta A_\parallel/(m_e c)$, $\phi^* = \phi - \mathbf{v}\cdot\delta\mathbf{A}/c$, $\bar{f}_i$ and $\bar{F}_e$ are the equilibrium ion and gyrokinetic electron velocity distribution functions, the operator $\langle\ldots\rangle$ represents gyroaveraging.

Assuming the condition $|\nabla_\perp^2| \gg |\nabla_\parallel^2|$, the generalized gyrokinetic Poisson's equation for the perturbed scalar potential ϕ can be written as

$$\left[\left(1 + \bar{\beta}_e + \frac{\bar{\omega}_{pe}^2}{\bar{\Omega}_e^2}\right)\nabla_\perp^2 - \frac{\bar{\omega}_{pi}^2}{\bar{V}_A^2}\right]\delta\phi = -4\pi\left[(1+\bar{\beta}_e)(q_i\delta n_i + q_e\langle\delta N_e\rangle) - \frac{4\pi\bar{n}_i q_i}{\bar{B}^2}\delta\Psi\right], \tag{5}$$

where $\bar{\omega}_{pe}$ and $\bar{\Omega}_e$ are, respectively, the electron plasma frequency and electron gyrofrequency based on the dc magnetic field and plasma density. The perturbed ion density δn_i is obtained by calculating the zeroth moment according to W_i in the discrete phase space, deposited to a mesh of spatial grids. The perturbed electron density $\langle\delta N_e\rangle$ is obtained by calculating the zeroth moment according to the four point gyroaveraged W_e. The quantity $\delta\Psi$ (Ref. 30) in Eq. (4) can be obtained from

$$\nabla^2\delta\Psi = -\nabla\cdot\left[\nabla\cdot\langle\delta\mathbf{P}_g\rangle + \frac{1}{c}\delta\mathbf{J}_i\times\mathbf{B} + \frac{1}{c}\mathbf{J}_i\times\delta\mathbf{B}\right], \tag{6}$$

where $\delta\mathbf{J}_i = q_i\int\mathbf{v}\delta f_i d^3\mathbf{v}$, $\mathbf{J}_i = q_i\int\mathbf{v}\bar{f}_i d^3\mathbf{v}$, and $\langle\delta\mathbf{P}_g\rangle = \int m_e\mathbf{v}\mathbf{v}\delta F_e d^3\mathbf{v}$.

The perturbed potential $\delta A_\parallel$ is given by the following linearized parallel Ampère's law:

$$\left(\nabla^2 - \frac{\omega_{pe}^2}{c^2}\right)\delta A_\parallel = -\frac{4\pi}{c}(\delta J_{i\parallel} + \langle\delta J_{e\parallel}\rangle), \tag{7}$$

where $\langle\delta J_{e\parallel}\rangle = (q_e/m_e)\int p_\parallel\delta F_e d^3\mathbf{v}$, and $\delta J_{i\parallel} = q_i\int v_\parallel\delta f_i d^3\mathbf{v}$. The perturbed parallel magnetic field $\delta B_\parallel$, meanwhile, is obtained from

$$\delta B_\parallel = 4\pi\frac{\delta\Psi + \bar{n}_i q_i(1+\rho_e^2\nabla_\perp^2)\delta\phi}{(1+\bar{\beta}_e)\bar{B}}. \tag{8}$$

The perturbed potential $\delta A_\perp$ is determined by the linearized perpendicular Ampère's law

$$\nabla^2\delta\mathbf{A}_\perp = -\frac{4\pi}{c}\delta\mathbf{J}_\perp, \tag{9}$$

with $\delta J_\perp = (c/4\pi)\nabla\times(\delta B_\parallel\bar{\mathbf{b}})$. Let $\delta\mathbf{A} = \delta A_\parallel\bar{\mathbf{b}} + \delta\mathbf{A}_\perp + \nabla_\perp\xi$. To ensure the Coulomb gauge condition $\nabla\cdot\delta\mathbf{A} = 0$, ξ must satisfy

$$\nabla_\perp^2\xi = -\nabla\cdot(\delta A_\parallel\bar{\mathbf{b}}). \tag{10}$$

The perturbed electric field can be obtained from the electron force balance equation

$$\bar{n}_e q_e\delta\mathbf{E} = \nabla\cdot\delta\mathbf{P}_e - \frac{1}{c}(\bar{\mathbf{J}}_e\times\delta\mathbf{B} + \delta\mathbf{J}_e\times\bar{\mathbf{B}}). \tag{11}$$

The calculated $\delta\mathbf{E}$ and $\delta\mathbf{B} = \nabla\times\delta A$ are then used to advance the ion weighting function W_i, and meanwhile, $\delta A_\parallel$ and $\delta\phi$ are used to advance the electron weighting function W_e.

B. Initial and boundary conditions

To exclude the tearing mode instability, the simulation is performed in the 2D yz plane, with z being along the current sheet normal and the antiparallel field component B_x perpendicular to the simulation plane. The initial magnetic field

TABLE I. Typical parameters for generation of current sheet instabilities.

Case: Dominant by:	Case 1 Mode A	Case 2 Mode B	Case 3 Mode C	Case 4 Modes A and B	Case 5 Modes B and C	Case 6 Mode D
B_G/B_{x0}	0.1	0.2	0.25	0.2	0.2	5
$k_y\rho_i$	6.8	6.8	2.7	6.8	6.8	0.16
n_{b0}	1.0	0.5	0.5	0.9	0.75	1.5
n_H	2.7	2.6	2.56	2.6	2.6	1.92
L/ρ_i	0.25	0.25	0.25	0.25	0.25	0.5
β_0	0.033	0.033	0.033	0.033	0.033	0.01
T_i/T_e	10	10	10	10	10	1
ω_{pe}/Ω_e	10	10	10	10	10	2.33

$$\mathbf{B}(z) = \hat{\mathbf{x}} B_{x0} \tanh(z/L) + \hat{\mathbf{y}} B_G, \tag{12}$$

where L is the half-width of the initial current sheet. We assume that initial temperatures T_i and T_e are constant everywhere in the domain.

Assume that the background and the Harris sheet plasmas have the same temperature. For a given ion beta value β_{i0}, defined with respect to the asymptotic field, the initial density in the Harris sheet is expressed as

$$n_{i0} = n_H \operatorname{sech}^2(z/L) + n_{b0}, \tag{13}$$

where n_{b0} is the background density, and the peak ion density n_H in the current sheet is obtained from the total pressure balance

$$n_H(T_i + T_e) = \frac{1}{8\pi} B_{x0}^2, \tag{14}$$

where T_i and T_e are in units of energy. The equilibrium velocity distribution of the Harris current sheet ion population is given by

$$\bar{f}_{Hi} = \frac{n_{h0}}{(2\pi T_i/m_i)^{3/2}} e^{-m_i\left[v_x^2+(v_y - V_{di})^2+v_z^2\right]/2T_i} \cdot e^{-V_{di}q_iA_y(z)/T_i}, \tag{15}$$

where V_{di} is the ion drift speed, and

$$n_{h0} e^{-V_{di}q_iA_y(z)/T_i} = n_{ih0}(z) = n_H \operatorname{sech}^2(z/L). \tag{16}$$

The background electron density is also chosen as n_{b0}. A Maxwellian velocity distribution is assumed for the background ion and electron populations. Initially, the GK electron equilibrium distribution function for the Harris sheet electrons takes the form (see the Appendix)

$$\bar{F}_{He,g} = \frac{n_{ih0}}{(2\pi T_e/m_e)^{3/2}} \exp\left(-\frac{B_x^2}{B^2}\frac{m_e V_{de}^2}{2T_e}\right)\left(1 - \frac{m_e V_{de}}{T_e \Omega_e}\frac{dB_x}{dz}\mu\right) \times \exp\left\{-\frac{1}{2T_e}\left[2\mu B + m_e\left(v_\parallel - \frac{V_{de}B_G}{B}\right)^2\right]\right\}, \tag{17}$$

where V_{de} is the electron drift speed. For the Harris sheet, $V_{de}/T_e = -V_{di}/T_i$. Note that the initial distribution functions given above are taken as the equilibrium distributions to be used in the δf calculations.

In the simulation, plasma density is normalized to $n_0 \equiv 100$ particles per grid cell, and magnetic field is normalized to $B_0 \equiv \sqrt{B_{x0}^2 + B_G^2}$. In the following, all quantities are presented as normalized ones. The parameters used in the simulation are described as follows. The normalized background density $n_{b0}=0.1-2$, while $n_H=1-4$ in the cases shown. The half-width of the current sheet $L=0.125-1\rho_i$, where ρ_i is the ion Larmor radius in the asymptotic magnetic field B_0. The system lengths are chosen as $l_y=0.5-100\rho_i$ in the y direction and $l_z=5.0-40\rho_i$ in the z direction. The grid number $N_y \times N_z = 32 \times 128 - 64 \times 512$. The electron temperature $T_e=0.1-1T_i$. The guide field $B_G/B_{x0}=0.05-10$. The electron beta $\beta_{e0}=n_{b0}\beta_0=0.01-0.2$ and ion beta $\beta_{i0}=n_{b0}T_i/T_e\beta_0=0.1-2$, where $\beta_0=n_0T_e/(B_0^2/8\pi)$. The simulations have been run in a wide range of $k_y\rho_i=0.1-40$. Some other dimensionless parameters are

$$\frac{m_i}{m_e} = 1836, \quad \frac{\omega_{pe}}{\Omega_e} = 2.2 - 10, \tag{18}$$

where $\omega_{pe}=(4\pi n_0 e^2/m_e)^{1/2}$ and $\Omega_e = eB_0/m_e c$. Note that the ratio of light to Alfvén speed $c/V_A = \sqrt{m_i/m_e}\omega_{pe}/\Omega_e$. Periodic boundary conditions are applied at $y=0$, l_y. The conducting boundary conditions are applied at $z=\pm l_z/2$, with $\delta\varphi=0$ and $\delta\mathbf{A}=0$.

III. SIMULATION RESULTS

Cases with various B_G/B_{x0}, k_y, β_0, n_{b0}, T_e/T_i, and L have been run to investigate microinstabilities in the Harris current sheet. It is found in the simulation that for $B_G/B_{x0}<1$, three types of instability modes, namely, modes A, B, and C, can be excited in the current sheet. These three modes exhibit different wave properties with real frequencies around ω_{LH}, the lower-hybrid frequency in the asymptotic magnetic field. Typical simulation parameters for the generation of modes A, B, and C are shown in Table I. As B_G/B_{x0} further increases, modes with new features can be obtained. Six typical simulation runs are described below in detail.

A. Mode A

In case 1, the guide magnetic field $B_G=0.1B_{x0}$, and the half-width of current sheet $L=0.25\rho_i$. An unstable mode (mode A) is obtained. Figure 1(a) shows contours of fluctuations of magnetic field (B_x, B_y, B_z), electric field (E_x, E_y, E_z), plasma densities (n_i, n_e), and $|\nabla \cdot \delta\mathbf{E}|$ and $|\nabla \times \delta\mathbf{E}|$ for $k_y\rho_i$

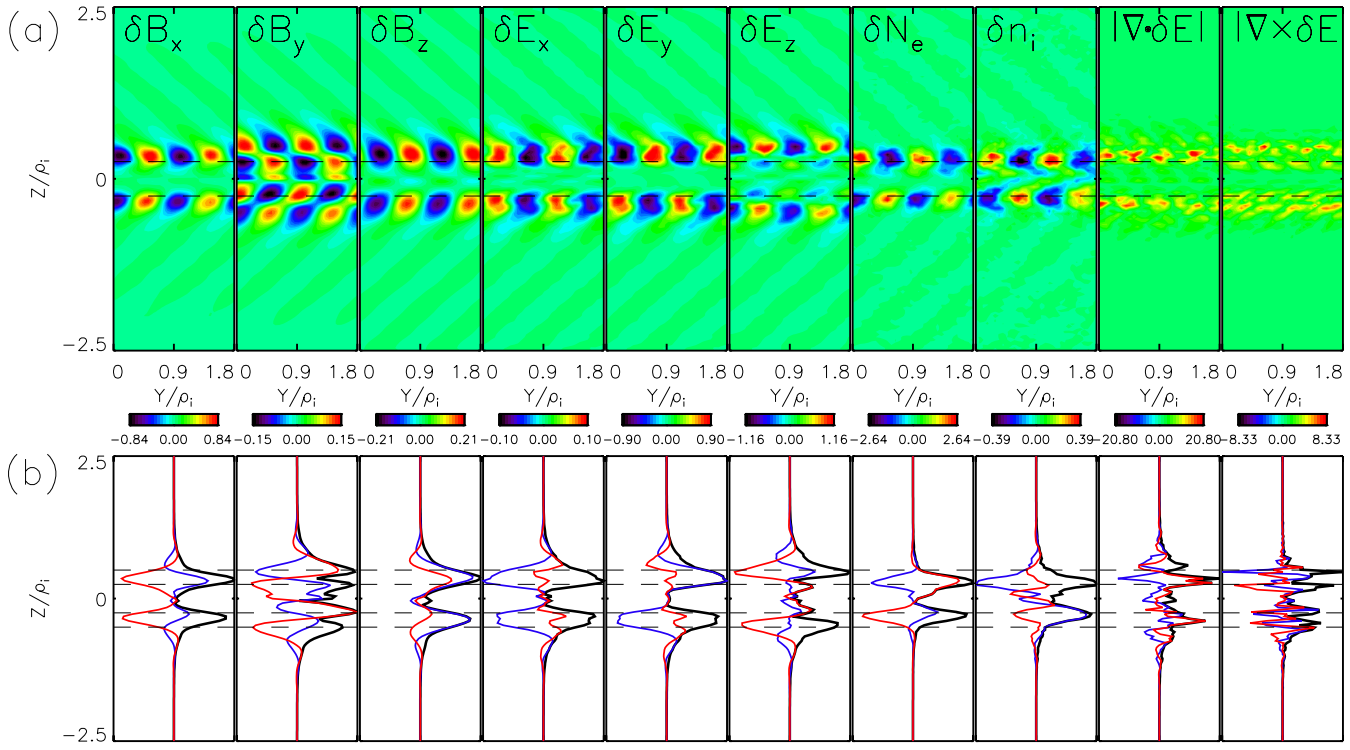

FIG. 1. (Color online) Simulation results of case 1 (mode A). (a) Contours of the perturbed electromagnetic field $(B_x, B_y, B_z, E_x, E_y, E_z)$, plasma density (n_i, N_e), $\nabla \cdot \mathbf{E}$, and $\nabla \times \mathbf{E}$ in the 2D simulation plane. The dashed lines mark $z = \pm L$, and scales in the colorbars are amplified by a factor of 10^4. (b) Eigenfunctions of corresponding quantities, where the red (blue, black) line represents the real (imaginary, absolute value) part. The dashed lines mark $z = \pm L$ and $\pm 2L$.

$=6.8$ in the 2D real space at $t=2\Omega_i^{-1}$. The dashed lines mark the positions of $z=\pm L$. It is seen that all the quantities except for δB_y are localized mainly near the current sheet edge. The maximum value of δB_x is four times that of δB_z, and both are present at $z=\pm 1.5L$. On the other hand, the fluctuation in B_y has a much smaller amplitude, and shows a wide structure. The maximum amplitude of δE_z is about the same order of that of δE_y and one order greater than that of δE_x. The fluctuation in the electron density is six times that in the ion density, and the maximum amplitude of the electron flow speed is found to be 30 times that of the ion speed. Note that the fluctuations of electron flow velocity $\delta \mathbf{U}_e$ are dominant by δU_{ex}, while that of ion velocity $\delta \mathbf{U}_i$ are dominant by δU_{iy}. The ion density fluctuation δn_i is in phase with the electron δN_e at the current sheet edge, $z=\pm L$.

The contours of $|\nabla \cdot \delta \mathbf{E}|$ and $|\nabla \times \delta \mathbf{E}|$ reveal, respectively, the electrostatic and electromagnetic properties of the instability. It is seen that in mode A, the maximum amplitude of the electrostatic component is larger than that of the electromagnetic component. The electrostatic component is localized mainly at $z=\pm 1.2-\pm 1.5L$, while the electromagnetic component is dominant at two locations with $z=\pm 1L$ and $z=\pm 1.5-\pm 2L$. The amplitude of $|\nabla \cdot \delta \mathbf{E}|$ is overall greater than $|\nabla \times \delta \mathbf{E}|$. The ratio of $|\nabla \cdot \delta \mathbf{E}|/|\nabla \times \delta \mathbf{E}| \sim 0.5-8$, and the average value of ratio $|\nabla \cdot \delta \mathbf{E}|/|\nabla \times \delta \mathbf{E}|$ is about 2 in the inner current sheet with $|z|<L$ and about 4 on the current sheet edge with $L<|z|<2L$. Therefore, mode A is quasielectrostatic on the current sheet edge, and has a non-negligible electromagnetic component in the center.

The eigenfunctions of mode A for various quantities are shown in Fig. 1(b). The dashed lines mark the positions of $z=\pm L$ and $\pm 2L$. The red (blue) line in Fig. 1(b) represents the real (imaginary) part of the corresponding quantity. Note that each quantity is scaled to the maximum of its absolute value. The black lines show the absolute values, which peak at current sheet edge within $L \leqslant |z| \leqslant 2L$. Again, mode A is localized on the current sheet edge.

The powers of the dominant field components δB_x and δE_z at different locations of z as a function of ω are presented in Fig. 2(a). In this case, the real frequency ω of mode

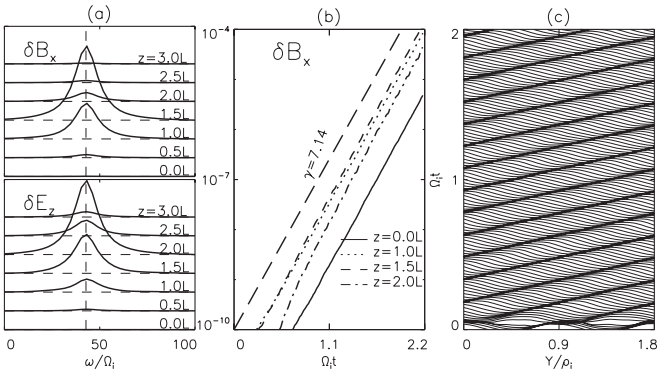

FIG. 2. Simulation results of case 1. (a) The relative powers of predominant components δB_x and δE_z, with $k_y \rho_i = 6.8$, as a function of real frequency at different locations of $z=0$, 0.5, 1, 1.5, 2, 2.5, and $3L$. The vertical dashed line marks the real frequency $\omega = 42.8\Omega_i$. (b) The power of δB_x with $k_y \rho_i = 6.8$ as a function of time at different locations at $z=0$, 1, 1.5, and $2L$. The long-dashed line represents $\sim e^{-\gamma}$ with $\gamma = 7.14$. (c) Time series plot of δB_x as a function of y at $z=1.5L$.

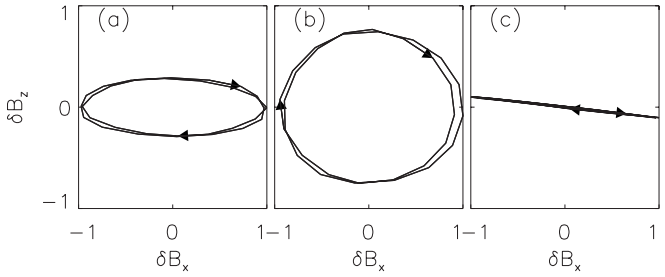

FIG. 3. Hodograms of magnetic field in δB_x-δB_z plane in (a) case 1 at $z=1.5L$, (b) case 2 at $z=0.5L$, and (c) case 3 at $z=0.5L$. The arrows indicate the direction from upstream to downstream against k_y. The field quantities are normalized to their maximum value in each case.

A is found to be $\omega \approx 42.8\Omega_i$, as marked by the dashed lines in Fig. 2(a). It is seen that the real frequency of mode A is independent of z, as expected for an eigenvalue. Figure 2(b) shows the amplitude of δB_x for mode A at locations of $z=0$, 0.25, 0.38, and $0.5\rho_i$, corresponding to $z=0$, L, $1.5L$, and $2L$, as a function of time. A linear growth rate γ_A is well established from the slopes of lines in Fig. 2(b). It is found that $\gamma_A=7.14\Omega_i$, which is also independent of z, again consistent with being an eigenmode. Mode A is found to be nonpropagating in the z direction, indicating a bounded state in z, and it only propagates in the $+y$ direction parallel to the ion drift velocity. Such propagation of mode A can also be seen from Fig. 2(c), the time series plot of perturbed magnetic field components δB_x as a function of y at $z=1.5L$. The phase speed of mode A is $V_{\mathrm{ph},A}=\omega/k_y=6.29v_{\mathrm{th}i}=0.782V_{di}$, where $v_{\mathrm{th}i}$ is ion thermal speed.

Figure 3(a) shows the hodograms of magnetic field in the δB_x-δB_z plane at $z=0.38\rho_i=1.5L$ for $t=2\Omega_i^{-1}$. The arrows in Fig. 3(a) indicate the direction from upstream to downstream against $\mathbf{k}_y$. Note that $\mathbf{B}_y>0$. It is seen that mode A has an elliptic right-hand polarization in magnetic field.

The structures obtained in case 1, with $k_y\rho_i=6.8$ corresponding to $k_yL=1.7$ and $k_y\sqrt{\rho_i\rho_e}=0.6$, have revealed properties that are similar to the LHDI structure obtained by Daughton.[11] It is well confined on the current sheet edge and dominated by δB_x. Nevertheless, the fact that electric fluctuation is dominated by δE_z and the electron velocity fluctuation is dominated by δU_{ex} may lead to a somewhat different conclusion. In case 1, the wave vector k_z is estimated to be $\sim 10/\rho_i$. Consider $B_x=0.995$ and $B_y=0.0995$ on the current sheet edge; the ratio $k_\parallel/k=(k_yB_y/\sqrt{B_x^2+B_y^2})/\sqrt{k_y^2+k_z^2} \approx 0.07 > \sqrt{m_e/m_i}$. The existence of finite $k_\parallel/k$ indicates that the mode is unlikely a pure LHDI mode. It is speculated that the instability associated with mode A is the modified two-stream/whistler instability,[6] or in the transition between LHDI and MTSI/whistler mode. The fact that the instability is located on the current sheet edge where $\beta \lesssim 1$ and V_d/V_A is moderate, i.e., $\simeq 2-5$, is also consistent with the MTSI/whistler mode.

1. k_y dependence

The eigenfunctions of magnetic and electric field for $k_y\rho_i=3.4$, 6.8, and 13.6 are shown in Fig. 4. Again, the fluctuations in electromagnetic fields are confined in a finite width in z around the edge on either side of the current sheet. It is seen that the width of the eigenfunctions increases with the decreasing wave number k_y. The locations of the peaks of perturbed magnetic field roughly remain unchanged with k_y. The peaks of electric field, however, shift outward as k_y increases from $k_y\rho_i=3.4$ to 13.6. The structures of electron plasma quantities (e.g., δN_e, and $\nabla\cdot\delta\vec{\mathbf{P}}_x$, not shown) are found to be almost unchanged with k_y.

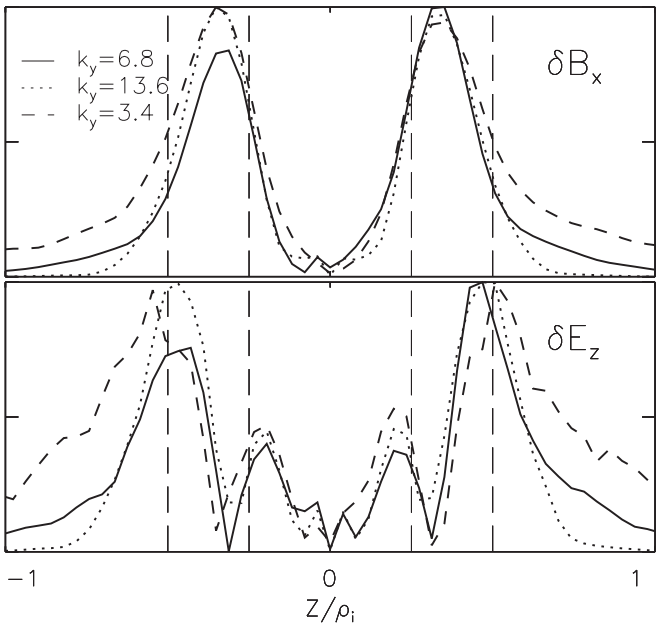

FIG. 4. Eigenfunctions of δB_x and δE_z with $k_y\rho_i=3.4$, 6.8, and 13.6 in mode A. The dashed lines mark $z=\pm L$ and $\pm 2L$.

Figure 5(a) shows the dispersion relation and growth rate of mode A as a function of k_y. For the cases with $B_G/B_{x0}=0.1$, mode A is unstable for $1.35<k_y\rho_i<26.9$. The maximum growth rate$=10.0\Omega_i$, and is found at $k_y\rho_i=15.6$, with the corresponding real frequency $\omega=95.24\Omega_i$. The dispersion relation of mode A in the range of $k_y\rho_i<25$ can nearly be expressed as $\omega=V_{\mathrm{ph}}k_y$, where $V_{\mathrm{ph}} \approx 0.78V_{di}$ is the phase speed of mode A.

2. β dependence

Cases with electron beta $\beta_{e0}=0.01-0.1$, corresponding to various electron and ion temperatures while maintaining $T_e/T_i=0.1$, have been simulated. The plasma beta is found to only slightly affect the perturbed electromagnetic field structures. The real frequency and growth rate as a function of β_{e0} are shown in Fig. 5(b). It is seen that the real frequency decreases with β_{e0}. The linear growth rate also decreases with β_{e0} when $\beta_{e0}>0.033$. Mode A is stable for $\beta_{i0} \gg 1$ in high-beta plasma, and is also stable if $\beta_{e0} \to 0$.

3. B_G dependence

It is seen from Fig. 5(a) that the range of k_y in which mode A is unstable is narrowed when the guide field B_G increases. The maximum growth rate $\gamma_{\max}$ becomes smaller with the increasing B_G/B_{x0}, and the location of the maximum growth rate shifts to smaller k_y. The phase speed V_{ph}, how-

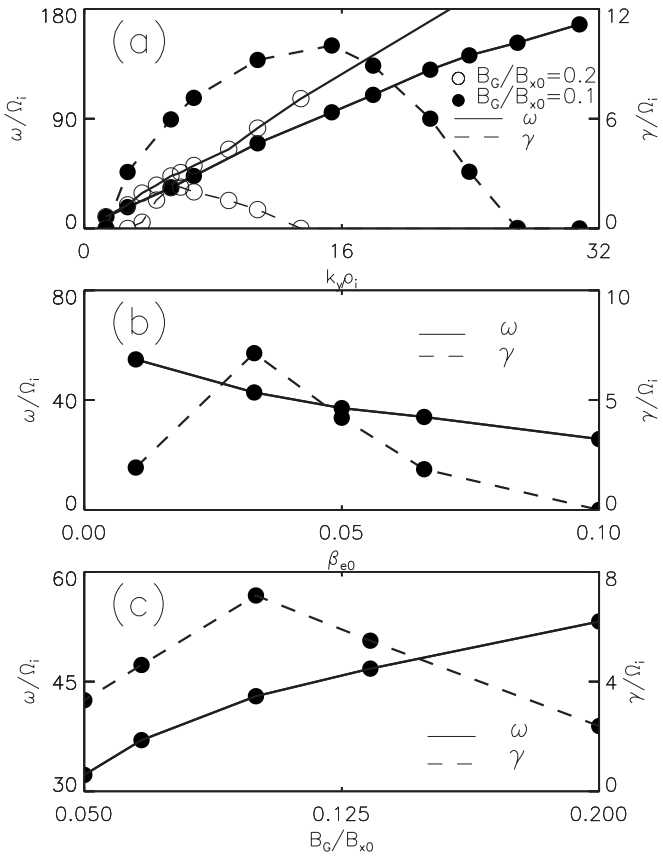

FIG. 5. Real frequency and growth rate of mode A (a) as a function of k_y for guide field $B_G/B_{x0}=0.1$ and 0.2 and $\beta_{e0}=0.033$, (b) as a function of electron β_{e0}, for $B_G/B_{x0}=0.1$ and $k_y\rho_i=6.8$ and (c) as a function of B_G for $k_y\rho_i=6.8$ and $\beta_{e0}=0.033$.

ever, increases with B_G/B_{x0}. The frequencies ω and γ as a function of B_G/B_x for $k_y=6.8$ are shown in Fig. 5(c). It is seen that the real frequency ω of mode A increases with B_G/B_{x0}. The eigenfunctions obtained in the simulation (not shown) indicate that the width of electromagnetic fluctuations in z become wider with the increasing B_G/B_{x0}.

B. Mode B

As the guide field increases and/or the ambient plasma beta (β_{e0} and β_{i0}) decreases, the current sheet instability is found to shift to the high-β region in the current sheet center, dominated by mode B. In case 2, in which $B_G/B_{x0}=0.2$ and $n_{b0}=0.5$, mode B is found to be dominant. Contours of various quantities at $t=2\Omega_i^{-1}$ are shown in Fig. 6(a). It is seen that the fluctuation of δB_y and δn are well confined in a narrow region at the current sheet center with $|z|<0.25L$, where $\beta_i \geqslant 10.5$. Fluctuations of other quantities are confined in the region with $|z| \leqslant L$. While δB_x dominates mode A in case 1, here δB_y and δE_z are dominant in mode B. The amplitude of δN_e is about the same as that of δn_i. The ion flow velocity is found to be primarily dominant by δU_{iy}, while δU_{ey} and δU_{ex} are stronger in the electron flow components. It is also seen from Fig. 6(a) that $|\nabla\cdot\delta\mathbf{E}|/|\nabla\times\delta\mathbf{E}|\approx 3$ in a very narrow region in the current sheet center with $|z|<0.25L$. The amplitudes of electrostatic and electromagnetic components are about the same order in all the other regions, with $|\nabla\cdot\delta\mathbf{E}|/|\nabla\times\delta\mathbf{E}|\sim 1$.

It has been argued in previous simulations that the LHDI, generated away from the neutral sheet, may not be able to penetrate into the current sheet center (e.g., Ozaki *et al.*[13]). Thus, it is questionable whether LHDI can contrib-

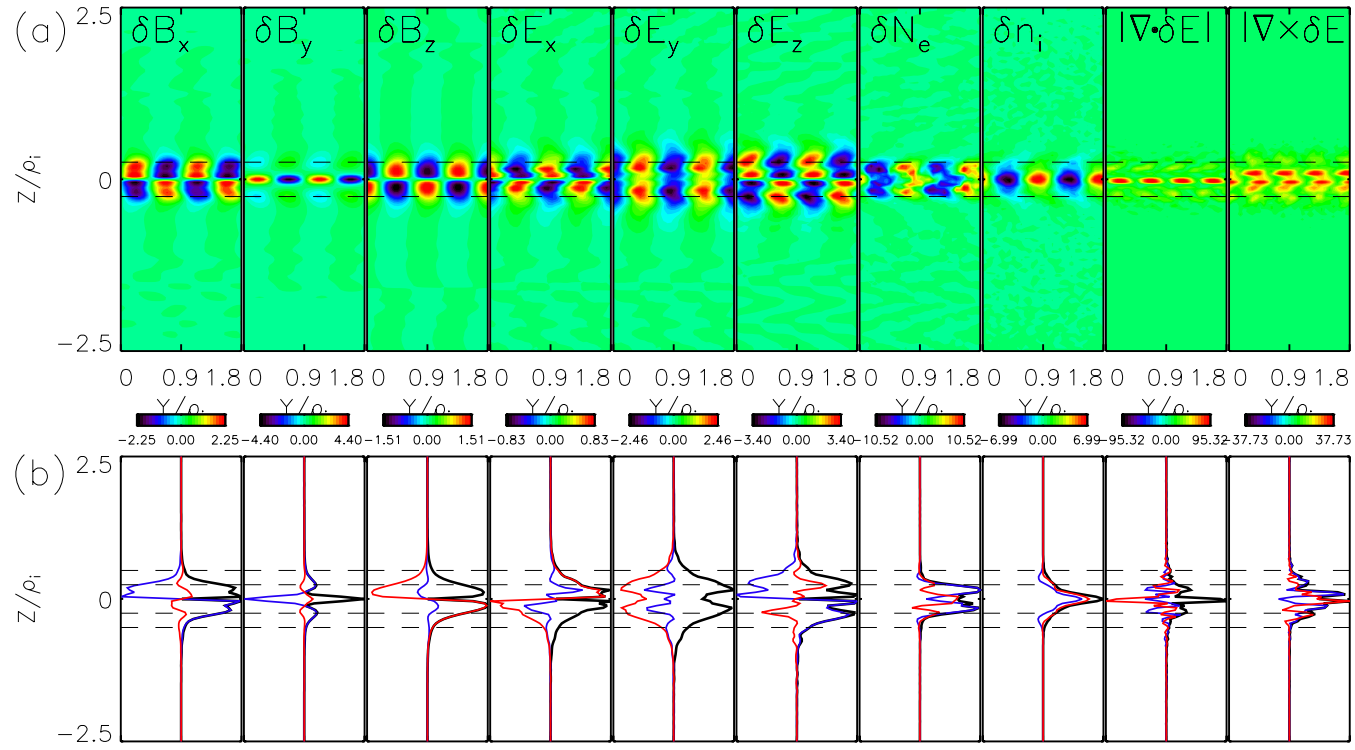

FIG. 6. (Color online) Simulation results of case 2 (mode B): (a) contours and (b) eigenfunctions of various quantities. The dashed lines in the top (bottom) panel mark $z=\pm L$ ($z=\pm L$ and $\pm 2L$). Scales in the colorbars are amplified by a factor of 10^8.

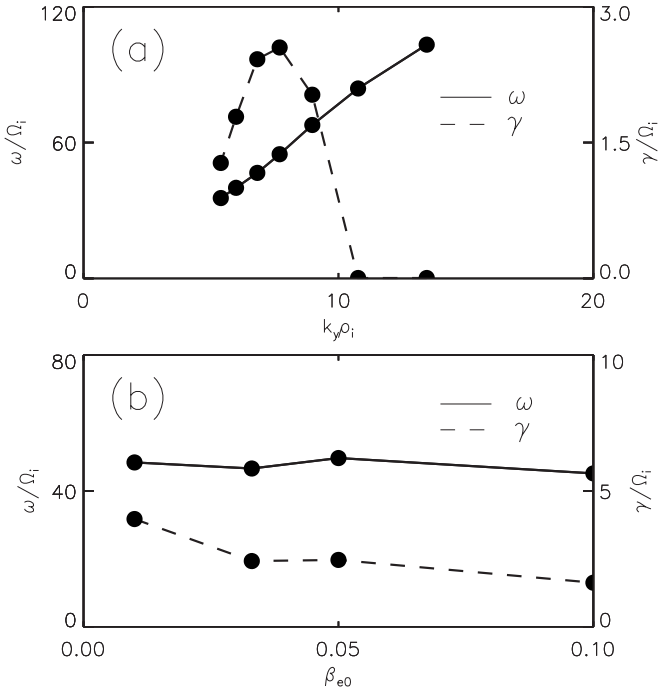

FIG. 7. Real frequency and growth rate of mode B (a) as a function of k_y for $B_G/B_{x0}=0.2$, $n_{b0}=0.5$, and $\beta_{e0}=0.016$ and (b) as a function of β_{e0} for $B_G/B_{x0}=0.2$, $n_{b0}=0.5$ and $k_y\rho_i=6.8$.

ute to the anomalous resistivity in magnetic reconnection. On the other hand, mode B obtained in our simulation is localized exactly in the current sheet center. It is associated with a larger compressional perturbation in B_y, along the direction of the electron drift velocity. It would be interesting to study the role of mode B in the anomalous resistivity in magnetic reconnection.

Figure 6(b) shows the eigenfunctions of various quantities in case 2. All fluctuations are clearly well confined in the current sheet. The quantities δB_y and δn_i peak at the neutral line at $z=0$. The perturbation δE_z exhibit an odd eigenfunction structure, while δE_y and δB_y have even eigenfunctions. The electron density, on the other hand, peaks near the current sheet edge at $z=\pm 0.75L$.

It is found that in case 2 the real frequency of mode B is $\omega=46.6\Omega_i$ and the linear growth rate $\gamma=2.34\Omega_i$. Similar to mode A, both ω and γ in mode B are also seen to be independent of z. Mode B only propagates in the y direction, with phase speed $V_{\mathrm{ph},B}=\omega/k_y=6.86v_{\mathrm{thi}}=0.84V_{di}$ in case 2.

The polarization of magnetic field components perpendicular to k_y can be found from Fig. 3(b), which shows the hodogram of magnetic field in the δB_x-δB_z plane at $z=0.125\rho_i=0.5L$ for $t=2\Omega_i^{-1}$. It is seen that mode B is right-hand and nearly circularly polarized in magnetic field.

Figure 7(a) shows the dispersion relation and growth rate as a function of k_y for mode B in the cases with $B_G/B_{x0}=0.2$ and $\beta_{e0}=0.016$. It is found that the maximum growth rate $\gamma_{\max}\approx 2.55\Omega_i$. The corresponding $k_{y,\max}\rho_i=7.69$ and $\omega_{\max}=54.8\Omega_i$. The width of $k_y\rho_i$ for unstable mode B is about 6, which is smaller than that of mode A in Fig. 5(a). When $k_y\rho_i<5$, mode B becomes stable with $\gamma=0$, while the instability is dominated by mode C, which is discussed below.

The frequencies ω and γ as a function of electron beta in mode B for $B_G/B_{x0}=0.2$ and $k_y\rho_i=6.8$ are shown in Fig. 7(b). It is seen that the real frequency ω is nearly unchanged with β_{e0}, while the growth rate γ decreases with β_{e0}. Note that when the asymptotic electron beta becomes higher with $\beta_{e0}>0.1$, the instabilities of mode A will become dominant, which exist on the low-β current sheet edge.

C. Mode C

As mentioned above, mode C is unstable for small k_y, as shown below in case 3 with $k_y\rho_i=2.69$ and $B_G/B_{x0}=0.25$. Figure 8(a) shows the contours of various quantities at $t=4\Omega_i^{-1}$. It is found that the magnetic field fluctuations are present everywhere in the current sheet region with $|z|<3L$, while the electric field fluctuations are mainly in the edge region with $L\leqslant|z|\leqslant 3L$. The electron density δN_e, however, is confined in a narrow region with $|z|\leqslant L$, while the maximum amplitude of δN_e is much greater than that of ion density δn_i. The fluctuation of δB_x is dominant in the magnetic field, while δE_z is dominant in the electric field. The ratio $|\nabla\cdot\delta\mathbf{E}|/|\nabla\times\delta\mathbf{E}|\approx 6$ on the current sheet edge with $|z|\sim 2L$, indicating that the fluctuations are highly electrostatic on the edge. The amplitudes of electrostatic and electromagnetic components are about the same order in the current sheet center, with $|\nabla\cdot\delta\mathbf{E}|/|\nabla\times\delta\mathbf{E}|\sim 1$.

Figure 8(b) shows the eigenfunctions of various quantities in case 3. It is seen that the region occupied by the electromagnetic field is wider than that in modes A and B. The phase differences between the real and imaginary parts of eigenfunctions are nearly 90° in mode C, while the phase differences are equal to 0° or 180° in modes A and B. Comparison between mode structures of E_z in cases 1 and 3 suggests that mode C is a higher eigenstate of mode A.

In this case, the real frequency is found to be $58.9\Omega_i$. The corresponding linear growth rate $\gamma=3.96\Omega_i$. Similar to modes A and B, the frequency of mode C is also independent of z, consistent with being a bounded eigenstate. The phase speed of mode C in case 3, along $+y$, is $V_{\mathrm{ph},C}=\omega/k_y=21.9v_{thi}=2.65V_{di}$, greater than the ion drift velocity V_{di}.

Figure 3(c) shows the hodograms of magnetic field in the δB_x-δB_z plane at $z=0.125\rho_i=0.5L$ for $t=4\Omega_i^{-1}$. It is seen that mode C is linearly polarized in magnetic field.

D. General cases with multiple modes

As described above, modes A, B, and C are unstable predominantly in different parameter regimes. The dependence of modes A, B, and C on the guide field B_G for the cases with background density $n_{b0}=0.5$, corresponding to $\beta_{i0}=0.16$ and $k_y\rho_i=6.8$, is shown in Fig. 9(a), in which the real frequency of each mode and the maximum growth rate obtained from the simulation are plotted. It is seen that in the cases with small guide field $B_G/B_{x0}\leqslant 0.1$, only mode A is excited. The growth rate of mode A decreases with B_G. As B_G increases, modes B and C appear. When B_G is the range of $0.12\leqslant B_G/B_0\leqslant 0.167$, modes A, B, and C are unstable

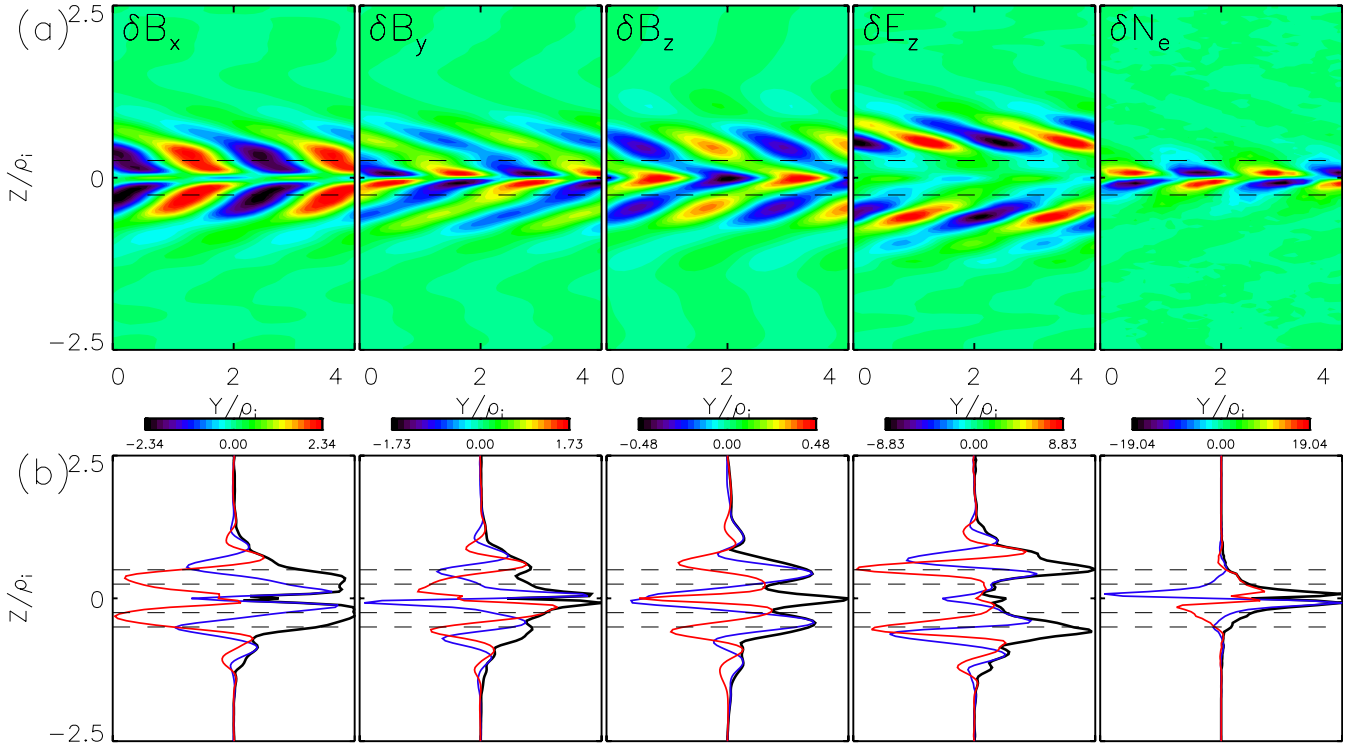

FIG. 8. (Color online) Simulation results of case 3 (mode C): (a) contours and (b) eigenfunctions of various quantities. The dashed lines in the top (bottom) panel mark $z=\pm L$ ($z=\pm L$ and $\pm 2L$). Scales in the colorbars are amplified by a factor of 10^3.

simultaneously in the current sheet. The frequency of mode B is the smallest among these three modes, while that of mode C is the highest. The frequency of mode A is close to that of mode B. When $B_G/B_{x0} \geqslant 0.2$, modes A and C are stabilized, and only mode B is generated and dominates the instability in the current sheet. The current sheet is then stabilized for all the modes when $B_G/B_{x0} \geqslant 0.5$.

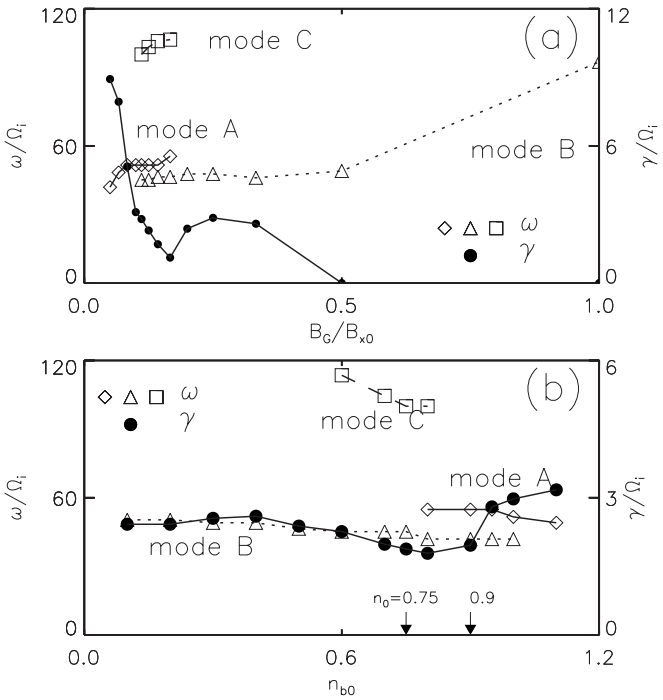

FIG. 9. Real frequency of modes A, B, and C and growth rate of eigenmode (a) as a function of B_G for $k_y\rho_i=6.8$, $n_{b0}=0.5$, and $\beta_{e0}=0.016$ and (b) as a function of n_{b0} for $k_y\rho_i=6.8$, $B_G/B_{x0}=0.2$, and $\beta_{e0}=0.016$.

Figure 9(b) shows frequencies and growth rates of the current sheet instabilities as a function of density n_{b0} for the cases with $B_G/B_{x0}=0.2$, $T_i/T_e=10$, and $k_y\rho_i=6.8$. Note that $n_{b0}=0.1-1$ corresponds to ion $\beta_{i0}=0.033-0.33$. It is seen that under a relatively high n_{b0}, only mode A is excited, with growth rate $\sim 3\Omega_i$. When n_{b0} decreases to $n_{b0} \leqslant 1.0$, mode B is also unstable. Mode B becomes stronger with the decreasing n_{b0}. When $n_{b0} \leqslant 0.8$, unstable mode C is also excited. When $0.6 \leqslant n_{b0} \leqslant 0.75$, modes B and C coexist in the system, while at $n_{b0} \approx 0.8$, all three modes exist simultaneously. Mode B gradually becomes the dominant instability as n_{b0} decreases.

As shown in Fig. 9, there can exist multiple modes simultaneously in general cases. Some examples with coexisting unstable modes A, B, and/or C are shown below. Figure 10(a) shows the powers of eigenmodes at different z-distances as a function of the real frequency in case 4 with $B_G/B_{x0}=0.2$ and $n_{b0}=0.9$. It is found in this case that the instabilities in the current sheet are governed by modes A and B. The frequency of mode A is $\omega_A=53.8\Omega_i$, which is larger than that of mode B with $\omega_B=43.5\Omega_i$. The fluctuations of mode B are present mainly at the center with $z\sim 0$, while the fluctuations of mode A are dominant on the current sheet edge with $z \geqslant L$. The powers of all quantities but δB_y in mode A are greater than those of mode B. The growth rate of mode B can be estimated by calculating the growth of δB_y localized at the current sheet center, while the growth rate of mode A can be determined by the growth of δB_x at the edge.

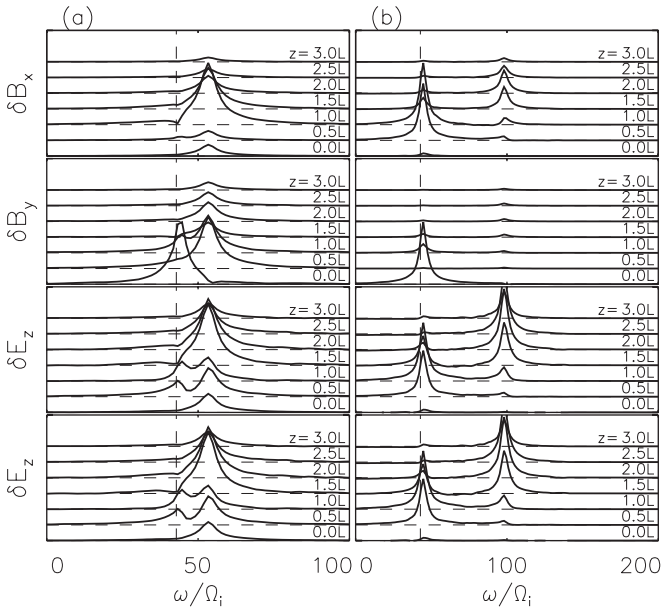

FIG. 10. The relative powers of perturbed electromagnetic quantities as a function of the real frequency at different z's for (a) case 4 and (b) case 5.

From the time dependence of δB_x and δB_y, we can obtain the growth rate of mode A as $\gamma_A \approx 2.1\Omega_i$ and that of mode B as $\gamma_B = 1.76\Omega_i$.

In case 5 with $B_G/B_{x0}=0.2$ and $n_{b0}=0.75$, as shown in Fig. 10(b), modes B and C are excited simultaneously. It is seen that the frequency of mode B is about $\omega_B = 45.1\Omega_i$, while the frequency of mode C is $\omega_C = 99.4\Omega_i > \omega_B$. It is clear that mode B dominates the instability in the current sheet center, and mode C is dominant outside the current sheet region with $|z| \geqslant 1.5L$. The growth rates of modes B and C in this case are $\gamma_B \approx \gamma_C \approx 1.89\Omega_i$.

E. Case with strong guide field

As B_G increases, $k_\perp$ and diamagnetic drift direction shift away from the current flow direction y. The location of maximum growth rate shifts to smaller k_y. In the situation with an extremely strong guide field, the instabilities generated in current sheet are found to become globally propagating. Figure 11(a) shows contours of various quantities in the 2D domain in case 6 with $B_G/B_{x0}=5.0$ at $t=4\Omega_i^{-1}$. A new mode, mode D, with a very small wave number $k_y\rho_i=0.16$ dominates the instability. Fluctuations of electromagnetic fields are seen throughout the region in $|z| \leqslant 4\rho_i = 8L$, which is different from the smaller-B_G cases shown above. The strength of electron density fluctuations is on the same order of that of ions. The maximum amplitude of $|\nabla \cdot \delta\mathbf{E}|$ is much larger than that of $|\nabla \times \delta\mathbf{E}|$, indicating that the instability is highly electrostatic. Figure 11(b) shows the "eigenfunctions" of various quantities. Note that unlike the standing wave bounded-state structures in previous cases with smaller B_G, mode D is not in a bounded eigenstate. It is generated in and propagates with time away from the current sheet. Similar to mode C, the real parts of the eigenmodes for electromagnetic fields have a nearly $\pm 90°$ phase difference with those of the imaginary parts. The plasma densities δN_e and δn_i are present

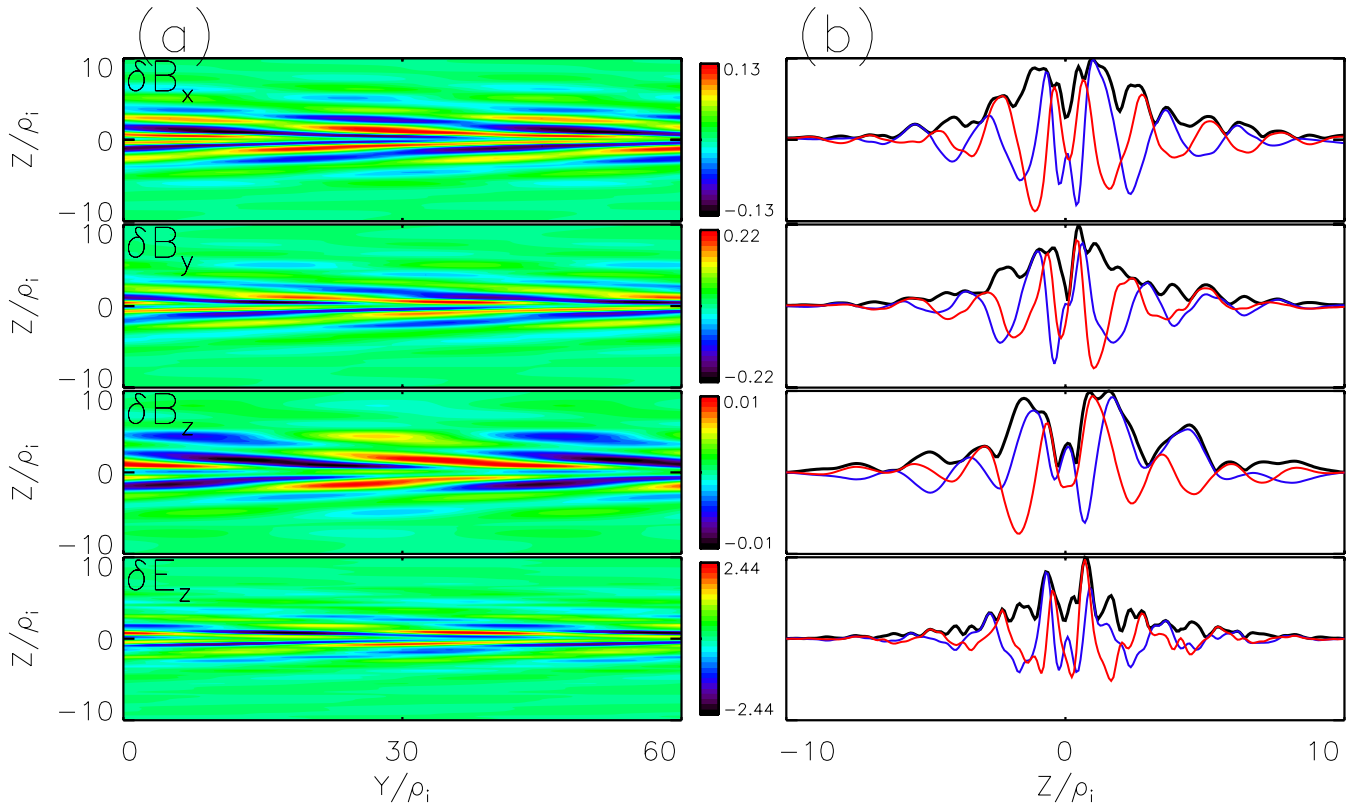

FIG. 11. (Color online) Simulation results of case 6 for extremely large guide field $B_G/B_{x0}=5$: (a) contours and (b) eigenfunctions of various quantities. Scales in the colorbars are amplified by a factor of 10^7.

mainly near the current sheet, with $|z| \leqslant L$, while the electron flow velocity $\delta \mathbf{U}_e$ is dominant in a wide region with $|z| \leqslant 8L$.

The real frequency of the instability in this case is found to be $43.1\Omega_i$, and the linear growth rate is about $1.58\Omega_i$. The mode is found to propagate not only in the y direction but also in $\pm z$, outward away from the current sheet. The phase speed of the mode is about $V_{\rm ph}=\omega/k_y=268.75v_{{\rm th}i}=12.9V_{di}$ in the y direction, and the phase speed in the z direction is about $8.54v_{ti}=0.41V_{di}$ near the current sheet with $|z|<1.5L$, and is equal to $16.78v_{ti}=0.8V_{di}$ in $|z|>1.5L$ outside.

Overall, our simulation shows that mode D has the following properties. Its wave number $k_\perp \rho_i \approx k_z \rho_i \sim 1$, and $k_\parallel / k_\perp \approx 0.05 \ll 1$. The real frequency $\omega \gg k_\parallel v_{{\rm th}e}$, while ω is near the harmonic of Ω_i, and the growth rate $\gamma \sim \Omega_i$. These suggest a streaming-ion excitation of electrostatic ion Bernstein/ion cyclotron instability.[33] The detailed physics for the strong guide field cases will be investigated elsewhere.

IV. SUMMARY

The instability of Harris current sheet is investigated using a linearized (δf) GKe/FKi code. The simulation is carried out in the 2D plane containing a finite guide field B_G (along y) and the current sheet normal (z), and is performed for a broad range of B_G.

It is found that for a finite B_G/B_{x0}, three unstable modes, i.e., modes A, B, and C, can be excited in the Harris current sheet. In the cases with a small B_G/B_{x0}, mode A is dominant. They are present mainly on the edge of the current sheet. The fluctuations are dominated by B_x, E_z and the electron density N_e. As B_G increases, mode A becomes weaker, and modes B and/or C are excited in the current sheet. In mode C, the perturbations of magnetic field, dominated by B_x, are extended from the current sheet center to 2–4 half-widths of the current sheet, while those of the electric field are mainly present on the near edge. The fluctuations in mode B, dominated by B_y and E_z, are localized at the current sheet center.

The real frequencies of modes A, B, and C, all in the range of the lower hybrid frequency, are in three different branches, with mode C having the highest frequency and mode B having the lowest. Mode A has the strongest growth rate among the three. Modes A and C are found to be predominantly electrostatic, while in mode B the electrostatic and electromagnetic fluctuations are of the same order. These three modes are found to propagate in the ion drift direction along $+y$. The phase speeds of modes A and B are below or equal to the ion drift speed, while that of mode C is greater than the ion drift speed. Mode A appears to be consistent with the MTSI/whistler mode, while mode C may be a higher eigenstate of mode A.

In the cases with extremely large $B_G/B_{x0} \gg 1$, the wave modes evolve to a globally propagating instability, while their real frequency is still around $\omega_{\rm LH}$. The fluctuations are dominated by B_y and E_z. The unstable modes may be the ion Bernstein/ion cyclotron instabilities. They are found to propagate not only in the current flow direction with phase speed much greater than the ion drift speed, but also outward along the current sheet normal, with speed less than the ion drift speed.

It is believed that collisionless magnetic reconnection requires an excitation of anomalous resistivity at the current sheet center, or the neutral point of magnetic field. Since the location where $\mathbf{k}\cdot\mathbf{B}=0$ can only be on the edge of the current sheet or outside the sheet center, it has been argued that the LHDI, whose maximum growth rate occurs at $\mathbf{k}\cdot\mathbf{B}=0$, may not be the direct cause for the anomalous resistivity. In the presence of a finite guide field B_G, we have found the existence of an unstable mode with $\mathbf{k}\cdot\mathbf{B}\neq 0$ at the center of the current sheet. In this mode, mode B, the wave perturbation in magnetic field is dominated by a compressional fluctuation δB_y in the direction of the electron drift velocity. It is speculated that mode B may contribute directly to the electron anomalous resistivity in magnetic reconnection.

LHDI instabilities was found in the previous particle simulations of current sheet (e.g., Daughton[11]). The simulation by Daughton was carried out in a tilted 2D plane such that $\mathbf{k}\cdot\mathbf{B}=0$ can be achieved on the edge of one side of the current sheet. On the other hand, our simulation is performed in the 2D plane with a constant (guide) field along y, and the MTSI/whistler mode with $\mathbf{k}\cdot\mathbf{B}\neq 0$ can be excited in the current sheet center where $\mathbf{B}\simeq\mathbf{B}_G\neq 0$. In fact, any instability at the current sheet center must have $\mathbf{k}\cdot\mathbf{B}\neq 0$. Nevertheless, the simulation by Daughton[11] also indicated that in the nonlinear stage, the LHDI waves excited on the current sheet edge can penetrate into the center of the sheet, and contribute to the anomalous resistivity. The nonlinear stage of evolution, however, is not included in our present simulation.

In the purely electrostatic limit, the results from our particle simulation model have been found to highly agree with an electrostatic local theory of Harris current sheet with a finite guide field.[32] We are, however, not aware of the existence of any nonlocal, electromagnetic theory of current sheet with a large guide field for comparison with the results shown in this paper. Finally, it should be noted that the physics of current sheet instability is a three-dimensional problem. In the presence of the finite B_G, it is expected that not only k_y, but k_x should also play an important role in the wave instability. Any 2D model can only address partial aspects of the evolution of current sheet.

ACKNOWLEDGMENTS

This work was supported by DOE Grant No. DE-FG02-05ER54826 to Auburn University and DOE Grant No. DE-FG03-94ER54736 and NSF Grant No. ATM-0335279 to UCI. Computer resources were provided by the NERSC supercomputer center and the Arctic Region Supercomputer Center (ARSC). The authors thank P. H. Yoon and W. Zhang for helpful discussions.

APPENDIX: GK ELECTRON EQUILIBRIUM DISTRIBUTION FUNCTION

The electron distribution in the velocity space can be written as

$$f_e = f_e(\varepsilon, p_x, p_y), \tag{A1}$$

where $\varepsilon = mv^2/2$, $p_x = mv_x + qA_x(z)$, $p_y = mv_y + qA_y(z)$. In the Harris current sheet with magnetic field $\mathbf{B}=B_G\hat{\mathbf{y}}+B_x(z)\hat{\mathbf{x}}$, the

equilibrium electron distribution function can be written as

$$f_{He} = \frac{n_{h0}}{(2\pi T_e/m_e)^{3/2}} e^{-\varepsilon/T_e} e^{V_{de} p_y/T_e}$$
$$= \frac{n_{h0}}{(2\pi T_e/m_e)^{3/2}} e^{-(m_e/2T_e)(v_x^2+v_z^2)} \cdot e^{-(m_e/2T_e)(v_y - V_{de})^2} \cdot e^{V_{de} q_e A_y/T_e + (1/2) m_e V_{de}^2/T_e}, \quad \text{(A2)}$$

where V_{de} is the electron drift speed in the y direction.

In the gyrocenter phase space, the guiding center electron distribution is represented as $F_g = F_g(\mu, v_\parallel, Z)$, where $Z = \hat{\mathbf{z}} \cdot \mathbf{X} = z + \rho \cdot \hat{\mathbf{z}}$, and $\rho = \mathbf{v} \times \mathbf{b}/\Omega$. Expanding to order $|\rho/L|^2$, where L is the half-width of the current sheet, and realizing $p_y = v_\parallel B_G/B(z) + A_y(z)$, the guiding center electron distribution function in the Harris sheet can be obtained as

$$F_{He,G} = \frac{n_{h0}}{(2\pi T_e/m_e)^{3/2}} e^{-\varepsilon/T_e} e^{V_{de}[m_e v_\parallel B_G/B + q_e A_y(z)]/T_e} \quad \text{(A3)}$$

$$= \frac{n_{h0}}{(2\pi T_e/m_e)^{3/2}} e^{-\mu B/T_e} e^{-(1/2) m_e (v_\parallel - V_{de} B_G/B)^2/T_e} \cdot e^{q_e V_{de} A_y(z)/T_e} \cdot e^{(1/2) m_e (V_0 B_G/B)^2/T_e} \quad \text{(A4)}$$

$$= \frac{n_{h0}}{(2\pi T_e/m_e)^{3/2}} e^{-(1/2T_e)[2\mu B + m_e (v_\parallel - V_{de} B_G/B)^2]} \cdot e^{-(B_G^2/B^2)(m_e V_{de}^2/2T_e)} \cdot e^{q_e V_{de} A_y(z)/T_e}, \quad \text{(A5)}$$

where $\varepsilon = [\mu B(z) + m_e v_\parallel^2]/2$, and $v_\parallel$ is the parallel velocity of particles.

The density $n(Z)$ obtained by integration of $F_{He,G}$, however, only corresponds to the guide center coordinates. But the charge neutrality requires $n_e(z) = n_i(z)$, where $n_e(z)$ is the electron density corresponding to the fully kinetic distribution. In order to calculate $n_e(z)$, we need to do an inverse transformation from the guiding center coordinates back to the six-dimensional $(\mathbf{x}, \mathbf{v})$ space. Noting that $Z = z + (\mathbf{v} \times \mathbf{b}/\Omega) \cdot \hat{\mathbf{z}} = z - (m/eB) v_\xi$, $\mathbf{b} = (1/B)[B_G \hat{\mathbf{y}} + B_x \hat{\mathbf{x}}]$, $\hat{\xi} = \mathbf{b} \times \hat{\mathbf{z}}$, $v_\parallel = v_y B_G/B - v_x B_x/B$, and $v_\xi = v_x B_G/B - v_y B_x/B$, for the electron distribution in Harris current sheet in the $(\mathbf{x}, \mathbf{v})$ space,

$$f_{He} = \frac{n_{h0}}{(2\pi T_e/m_e)^{3/2}} e^{-(m_e/2T_e)[(v_x^2+v_z^2)+(v_y - V_{de})^2]} e^{-(V_{de} q_e/T_e) A_y(z)}, \quad \text{(A6)}$$

the inverse transformation[34] leads to

$$T_g^{-1} F_{He,G} = f_{He} \cdot e^{-(V_{de} q_e/T_e) A_y''(z) \cdot (1/2)(m_e/q_e B)^2 v_\xi^2} \simeq F_{He}[1 - \delta_\nu], \quad \text{(A7)}$$

where

$$\delta_\nu = \frac{V_{0e} e}{T_e} A_y'' \frac{1}{2} \left(\frac{m}{eB} \right)^2 v_\xi^2.$$

Noticing $A_y' = \partial A_y/\partial z = -B_x$, $A_y'' = -\partial B_x/\partial z = -B_x'$, δ_ν can be expressed as

$$\delta_\nu = -\frac{m_e V_{de}}{T_e} \frac{B_x'}{B} \left(\frac{m_e}{q_e B} \right) v_\xi^2. \quad \text{(A8)}$$

Therefore, this δ_ν leads to error in $n_e(z)$ if the guiding center distribution F_{HG} is used to obtain the electron density. In the gyrokinetic approximation, we must include the effects of gyrophase averaging. The error in the GK approximation is then

$$\oint \frac{d\alpha}{2\pi} \delta\nu = -\frac{1}{2} \frac{m_e V_{de}}{T_e} \frac{B_x'}{B} \frac{1}{\Omega_e} v_\perp^2 = -\frac{m_e V_{de}}{T_e} \frac{B_x'}{\Omega_e} \mu. \quad \text{(A9)}$$

To offset this factor, the guiding center distribution function in Eq. (A5) must be modified as

$$F_{He,g} = \frac{n_{h0}}{(2\pi T_e/m_e)^{3/2}} e^{-(1/2T_e)[2\mu B + m_e (v_\parallel - V_{de} B_G/B)^2]} \cdot e^{-(B_x^2/B^2)(m_e V_{de}^2/2T_e)} \cdot e^{q_e V_{de} A_y(z)/T_e} \left[1 - \frac{m_e V_{de}}{T_e \Omega_e} \frac{dB_x}{dz} \mu \right]. \quad \text{(A10)}$$

Compared with Eq. (16) and considering $V_{de}/T_e = -V_{di}/T_i$, the GK electron distribution function in the Harris sheet can be written as

$$\bar{F}_{He,g} = \frac{n_{ih0}(Z)}{(2\pi T_e/m_e)^{3/2}} e^{-(B_x^2/B^2)(m_e V_{de}^2/2T_e)} \left(1 - \frac{m_e V_{de}}{T_e \Omega_e} \frac{dB_x}{dz} \mu \right) \times e^{-(1/2T_e)[2\mu B + m_e (v_\parallel - V_{de} B_G/B)^2]}. \quad \text{(A11)}$$

[1] J. W. Dungey, Phys. Rev. Lett. **6**, 47 (1961).
[2] N. A. Krall and M. N. Rosenbluth, Phys. Fluids **5**, 1435 (1962).
[3] T. A. Carter, M. Yamada, H. Ji, R. M. Kulsrud, and F. Trintchouk, Phys. Plasmas **9**, 3272 (2002).
[4] R. C. Davidson, N. T. Gladd, C. S. Wu, and J. D. Huba, Phys. Fluids **20**, 301 (1977).
[5] N. T. Gladd, Plasma Phys. **18**, 27 (1976).
[6] C. S. Wu, Y. M. Zhou, S. T. Tsai, and S. C. Gao, Phys. Fluids **26**, 1259 (1983).
[7] H. Sanuki, T. Watanabe, and M. Watanabe, Phys. Fluids **23**, 158 (1980).
[8] D. W. Ross and S. M. Mahajan, Phys. Rev. Lett. **40**, 324 (1978).
[9] J. D. Huba, J. F. Drake, and N. T. Gladd, Phys. Fluids **23**, 552 (1980).
[10] W. Daughton, Phys. Plasmas **6**, 1329 (1999).
[11] W. Daughton, Phys. Plasmas **10**, 3103 (2003).

[12]D. Winske, Phys. Fluids **24**, 1069 (1981).
[13]M. Ozaki, T. Sato, R. Horiuchi, and C. S. Group, Phys. Plasmas **3**, 2265 (1996).
[14]R. Horiuchi and T. Sato, Phys. Plasmas **6**, 4565 (1999).
[15]T. Moritaka, R. Horiuchi and H. Ohtani, Phys. Plasmas **14**, 102109 (2007).
[16]W. Daughton, G. Lapenta, and P. Ricci, Phys. Rev. Lett. **93**, 105004 (2004).
[17]P. Ricci, J. U. Brackbill, W. Doughton, and G. Lapenta, Phys. Plasmas **12**, 055901 (2005).
[18]P. Ricci, J. U. Brackbill, W. Doughton, and G. Lapenta, Phys. Plasmas **12**, 055901 (2005).
[19]J. F. Drake, R. G. Kleva, and M. E. Mandt, Phys. Rev. Lett. **73**, 1251 (1994).
[20]J. F. Drake, D. Biskamp, and A. Zeiler, Geophys. Res. Lett. **24**, 2921, DOI: 10.1029/97GL52961 (1997).
[21]P. Ricci, J. U. Brackbill, W. Doughton, and G. Lapenta, Phys. Plasmas **11**, 4102 (2004).
[22]C. A. Cattelll and F. S. Mozer, Geophys. Res. Lett. **13**, 221, DOI: 10.1029/GL013i003p00221 (1986).
[23]C. A. Cattelll and F. S. Mozer, in *Magnetotail Physics*, edited by A. T. Y. Lui (Johns Hopkins University Press, Baltimore, 1987), p. 119.
[24]I. Shinohara, T. Nagai, M. Fujimoto, T. Terasawa, T. Mukai, K. Tsuruda, T. Yamamoto, and J. Ricci, J. Geophys. Res. **103**, 20365, DOI: 10.1029/98JA01104 (1998).
[25]T. A. Carter, H. Ji, F. Trintchouk, M. Yamada, and R. M. Kulsurud, Phys. Rev. Lett. **88**, 015001 (2002).
[26]S. D. Bale, F. S. Mozer, and T. Phan, Geophys. Res. Lett. **29**, 2180, DOI: 10.1029/2002GL016113 (2002).
[27]X. H. Wei, J. B. Cao, G. Z. C. Zhou, O. Santolik, H. Reme, I. Dandouras, N. Cornilleau, E. Lucek, C. M. Carr, and A. Fazakerley, J. Geophys. Res. **89**, 2673, DOI: 10.1029/JA089iA05p02673 (1984).
[28]H. Ji, S. Terry, M. Yamada, R. Kulsrud, A. Kuritsyn, and Y. Ren, Phys. Rev. Lett. **92**, 115001 (2004).
[29]X. H. Deng and H. Matsumoto, Nature (London) **410**, 557 (2001).
[30]Y. Lin, X. Y. Wang, Z. Lin, and L. Chen, Plasma Phys. Controlled Fusion **47**, 657 (2005).
[31]S. E. Parker and W. W. Lee, Phys. Fluids B **5**, 77 (1993).
[32]P. H. Yoon, Y. Lin, X. Y. Wang, and A. T. Y. Lui, "Lower-hybrid drift instability for current sheet equilibrium with guide field", J. Geophys. Res. (unpublished).
[33]T. H. Stix, *Waves in Plasmas* (American Institute of Physics, Melville, NY, 1992).
[34]L. Chen, *Waves and Instabilities in Plasmas* (World Scientific, Singapore, 1987).